JGR Atmospheres

RESEARCH ARTICLE
10.1029/2021JD036424

Key Points:

- An intense and stationary cyclone around the ice shelf, which was part of a wave train occurred at the time of the calving
- Strong near-surface winds associated with the cyclone promoted the calving of the Brunt Ice Shelf via oceanward sea-surface slope
- Calving occurred on 26 February when the ice accelerated significantly in a westward direction from a velocity of 4–6 to 700 m day^{-1}

Correspondence to:

D. Francis,
diana.francis@ku.ac.ae

Citation:

Francis, D., Fonseca, R., Mattingly, K. S., Marsh, O. J., Lhermitte, S., & Cherif, C. (2022). Atmospheric triggers of the Brunt Ice Shelf calving in February 2021. *Journal of Geophysical Research: Atmospheres*, *127*, e2021JD036424. https://doi.org/10.1029/2021JD036424

Received 29 DEC 2021
Accepted 13 MAY 2022

Author Contributions:

Conceptualization: Diana Francis
Data curation: Ricardo Fonseca, Kyle S. Mattingly, Oliver J. Marsh, Stef Lhermitte
Formal analysis: Ricardo Fonseca, Kyle S. Mattingly, Oliver J. Marsh, Stef Lhermitte
Funding acquisition: Diana Francis
Investigation: Ricardo Fonseca
Methodology: Diana Francis
Project Administration: Diana Francis
Resources: Oliver J. Marsh
Software: Charfeddine Cherif
Supervision: Diana Francis
Validation: Diana Francis
Visualization: Ricardo Fonseca, Kyle S. Mattingly, Stef Lhermitte, Charfeddine Cherif
Writing – original draft: Ricardo Fonseca
Writing – review & editing: Diana Francis

Atmospheric Triggers of the Brunt Ice Shelf Calving in February 2021

Diana Francis[1], Ricardo Fonseca[1], Kyle S. Mattingly[2], Oliver J. Marsh[3], Stef Lhermitte[4], and Charfeddine Cherif[1]

[1]Environmental and Geophysical Sciences (ENGEOS) Lab, Khalifa University, Abu Dhabi, United Arab Emirates, [2]Space Science and Engineering Center, University of Wisconsin-Madison, Madison, WI, USA, [3]British Antarctic Survey, Cambridge, UK, [4]Department of Geoscience and Remote Sensing, Delft University of Technology, Delft, The Netherlands

Abstract The calving of Antarctic ice shelves remains unpredictable to date due to a lack of understanding of the role of the different climatic components in such events. In this study, the role of atmospheric forcing in the calving of the Brunt Ice Shelf (BIS) in February 2021 is investigated using a combination of observational and reanalysis data. The occurrence of a series of extreme cyclones around the time of the calving induced an oceanward sea-surface slope of >0.08° leading to the calving along a pre-existing rift. The severe storms were sustained by the development of a pressure dipole on both sides of the BIS associated with a La Niña event and the positive phase of the Southern Annular Mode. Poleward advection of warm and moist low-latitude air over the BIS area just before the calving was also observed in association with atmospheric rivers accompanying the cyclones. Immediately after the calving, strong offshore winds continued and promoted the drift of the iceberg A-74 in the Weddell Sea at a speed up to 700 m day^{-1}. This study highlights the contribution of local atmospheric conditions to ice-shelf dynamics. The link to the larger scale circulation patterns indicates that both need to be accounted for in the projections of Antarctic ice shelf evolution.

Plain Language Summary A calving event is the process by which a large block of ice gets separated from an ice shelf or glacier and forms an iceberg. Large calving events from marine-terminating ice shelves around Antarctica remain to date highly unpredictable. This process is typically associated with the glaciological cycle of the ice shelves as well as ocean dynamics. However, atmospheric forcing in triggering such events has been largely overlooked. This is investigated for the calving of iceberg A-74 from the Brunt Ice Shelf (BIS) in February 2021. We found that strong near-surface winds associated with intense cyclones promoted the event via an increased sea-surface slope toward the open ocean, which amplified the stress on the pre-existing rift and led to the calving. After the calving, the iceberg drifted westwards in the Weddell Sea at a speed of 700 m day^{-1} aided by strong offshore winds. The extreme weather conditions leading to the calving were associated with an alternation of a series of high (blockings) and low (troughs) pressure systems around the BIS region.

1. Introduction

Ice shelves and floating ice tongues around Antarctica extend cover an area larger than 1.561 million km^2, corresponding to 11% of Antarctica's total area (Rignot et al., 2013). Over the last decades, ice shelves have been retreating significantly or collapsed altogether, with a reduction in the ice-shelf area of >28,000 km^2 around the Antarctic Peninsula alone (Cook & Vaughan, 2010). The Antarctic Ice Sheet as a whole has experienced a 10-fold increase in ice loss from the 1990s to the late 2000s, with values jumping from 25 to 300 km^3 year^{-1} (Paolo et al., 2015). The land ice loss has important implications for sea-level rise both globally and regionally (e.g., Wadhams & Munk, 2004). In fact, ice shelves around Antarctica act as a buffer for the land ice behind, shielding it from ocean swells that may promote ice ablation. When ice shelves weaken or collapse, locally ice loss accelerates, enabling sea-level rise (Massom et al., 2018). Recent climate studies have noted the increased vulnerability of the Antarctic ice shelves (Gilbert & Kittel, 2021; Stammerjohn et al., 2021), where basal melt by an increasingly warmer ocean can promote ice loss from ice shelves (Gwyther et al., 2020; Rignot et al., 2013).

Ice shelf calving occurs when a fracture in the ice shelf extends over its full thickness, allowing for a chunk of ice to detach and float away (e.g., Alley et al., 2008; Benn et al., 2007). Over the last couple of decades, several Antarctic ice shelves have experienced major calving events. Examples include the Amery Ice Shelf in 2019

(Francis et al., 2021), the Larsen C Ice Shelf in 2017 (Hogg & Gudmudsson, 2017), the demise of the Pine Island Glacier (Lhermitte et al., 2020), and the Brunt Ice Shelf (BIS) in February 2021 (Larter, 2022). Most of the studies on ice shelf calving focus on ocean dynamics, targeting aspects such as the role of ocean swells (Massom et al., 2018), the warming and expansion of the Circumpolar Deep Water (Cook et al., 2016; Larter, 2022), the hydrofracturing mechanism and its role in the destabilization of ice shelves (Rott et al., 1996; Scambos et al., 2000, 2003, 2009), and the penetration of Antarctic Surface Water into shelf cavities (Stewart et al., 2019). On top of the ocean and the glaciological factors which precondition ice shelves for calving over long periods of time, the atmospheric forcing may also play a role during the calving events. For instance, atmospheric forcing can trigger ice shelf calving events (e.g., Francis et al., 2021) and can be reinforced by large-scale circulation anomalies such as the zonal wavenumber 3 pattern which regularly occurs in the Southern Hemisphere midlatitudes (Francis et al., 2019, 2020). Francis et al. (2021) reports on the crucial role that atmospheric conditions played in the September 2019 calving of the Amery Ice Shelf. A blocking pattern led to stationary cyclones at the front of the Amery Ice Shelf. This resulted in strong and persistent winds which promoted the ice calving by creating a steep sea-surface slope toward the ocean.

In late February 2021, the iceberg A-74, with a surface area of roughly 1,270 km^2, calved from the north side of the BIS (Figures 1a and 1b), and during March 2021 gradually drifted into the open ocean (Figures 1c and 1d). No sea-ice was present during this period as the event took place in the austral summer season. Although most of the ice loss at the BIS over the last decade has been attributed to the inflow of warm ocean water (Larter, 2022) and to a glaciological cyclic processes (De Rydt et al., 2019), the atmospheric forcing may have played a role in triggering the February 2021 calving event. Therefore, the goal of this paper is to investigate the role of atmospheric conditions together with the state of the ocean and ice in the A-74 calving event in February 2021. This paper is structured as follows. In Section 2, the data sets used in this study are described. In Section 3, the large-scale atmospheric environment is examined, whereas the atmospheric conditions around the BIS region are analyzed. In Section 4, the ocean and ice conditions before and after the calving are described. The main findings of this study are discussed in Section 5.

2. Data and Methods

In this section, the data sets considered and the methodology followed are summarized.

2.1. Satellite Observations

Two satellite-derived products are employed in this study. Visible images collected by the Moderate Resolution Imaging Spectroradiometer (MODIS; Xiong & Barnes, 2006) instrument on board the National Aeronautic and Space Administration's Terra and Aqua satellites are used to inspect the evolution of the BIS and the calving of the iceberg A-74. The displacement of the iceberg is assessed through the analysis of the panchromatic band 8 of the Landsat satellite, which is sensitive to wavelengths in the range 0.50–0.68 μm and provides images at a spatial resolution of 15 m (Fahnestock et al., 2016). The change detection technique considered is based on an unsupervised classification with two classes (Tian et al., 2020), water and ice, applied to Landsat 8 images between 15 October 2020 and 17 March 2021.

2.2. Ground-Based Observations

In situ measurements, collected at the Halley Research Station (Halley VI a) located at 75.5681°S and 25.5083°W on the BIS during February 2021, are used to analyze the local atmospheric conditions and assess their potential role on the calving. Fields measured on an hourly basis include the 2-m temperature and relative humidity, and the 10-m horizontal wind direction and speed. Single-frequency Global Positioning System (GPS) data are recorded on the ice shelf prior to the calving and on the iceberg following the calving. Data are recorded at hourly intervals, allowing the timing of the calving to be determined at high precision.

2.3. Reanalysis Data

The main reanalysis data set used in this study is ERA-5 (Hersbach et al., 2020). It is the most recent reanalysis developed by the European Centre for Medium-Range Weather Forecasts, and is available on a 0.25° × 0.25°

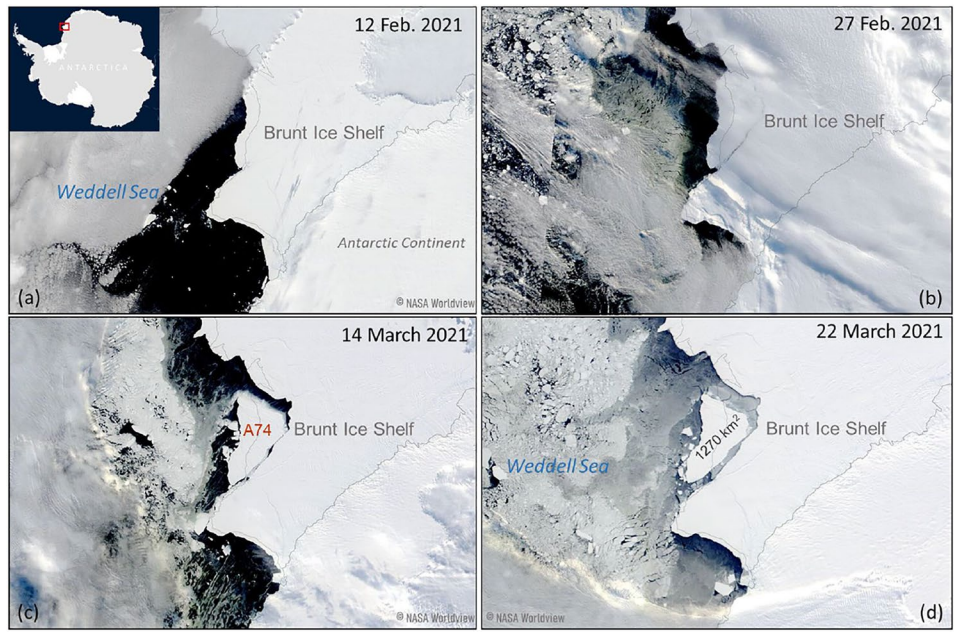

Figure 1. MODIS visible satellite images on (a) 12 February, (b) 27 February, (c) 14 March, and (d) 22 March 2021 over the Brunt Ice Shelf (BIS) in the Weddell Sea sector of Antarctica. The iceberg A-74 calved in late February and drifted away from the BIS in March 2021. Image credits: NASA Worldview.

(~27 km) grid and on an hourly basis. ERA-5 has been found to be one of the best performing reanalyzes in the Southern Hemisphere around Antarctica (e.g., Dong et al., 2020). For the spatial maps, daily mean data, computed from 3-hourly files, are used for both surface and pressure-level fields. The anomalies are calculated relative to all February months in the 1979–2020 climatological period (the standard deviation is extracted in the same way). For the histograms, 3-hourly wind speed values within ±15 Julian days of the calving date and for the period 1979–2020 (climatology) at a given grid-point in the domain 24°–28°W and 74.8°–75.8°S are considered. Besides standard fields, and in order to better understand the large-scale circulation around the time of the calving, the wave activity (*W*) vectors from Takaya and Nakamura (2001), which are shown to be parallel to the group velocity of Rossby waves in the plane wave limit, are plotted.

The ocean slopes are computed from the Hybrid Coordinate Ocean Model (HYCOM; Cummings & Smedstad, 2013) reanalysis data set, which provides several ocean-related fields on a roughly 0.08° (~9 km) grid between 80.48°S and 80.48°N and on a 3-hourly basis. The slopes are derived from the HYCOM sea-surface elevation by computing the local gradient using the 4-connected neighbors of each pixel. Based on these per pixel slopes, time series of region-wide mean slope values are derived by computing the average slope per time step for a ~10-km wide area surrounding the BIS (indicated by a red polygon in Figure 8c). Additionally, a map of maximum slope anomaly values corresponding to the calving event is calculated as the maximum ocean slope anomaly (°) for the period 15–28 February 2021 relative to April 2020 to March 2021.

3. The Large-Scale Atmospheric Environment

Figure 2 summarizes the large-scale circulation in the Southern Hemisphere in February 2021. The monthly mean sea-level pressure anomalies (Figure 2a) show a region of low pressure centered over the Bellinghausen/Amundsen Sea, where the pressure is lower than the 1979–2020 climatological mean by more than 1 standard deviation. This feature is a response to the La Niña that was present at the time (Yu et al., 2022). La Niña is the cold phase of the El Nino Southern Oscillation (ENSO; Rasmusson & Carpenter, 1982), which is a pattern of variability of the climate system with periods of 3–7 years with decadal variations. La Niña is characterized by colder than average sea-surface temperatures (SSTs) in the central and eastern equatorial Pacific, with typical amplitudes of 1–4°C. A La Niña started to develop in the austral spring of 2020, and persisted throughout the 2020/2021 austral summer season (Yu et al., 2022). As noted by Yuan (2004) and Simpkins et al. (2012), an

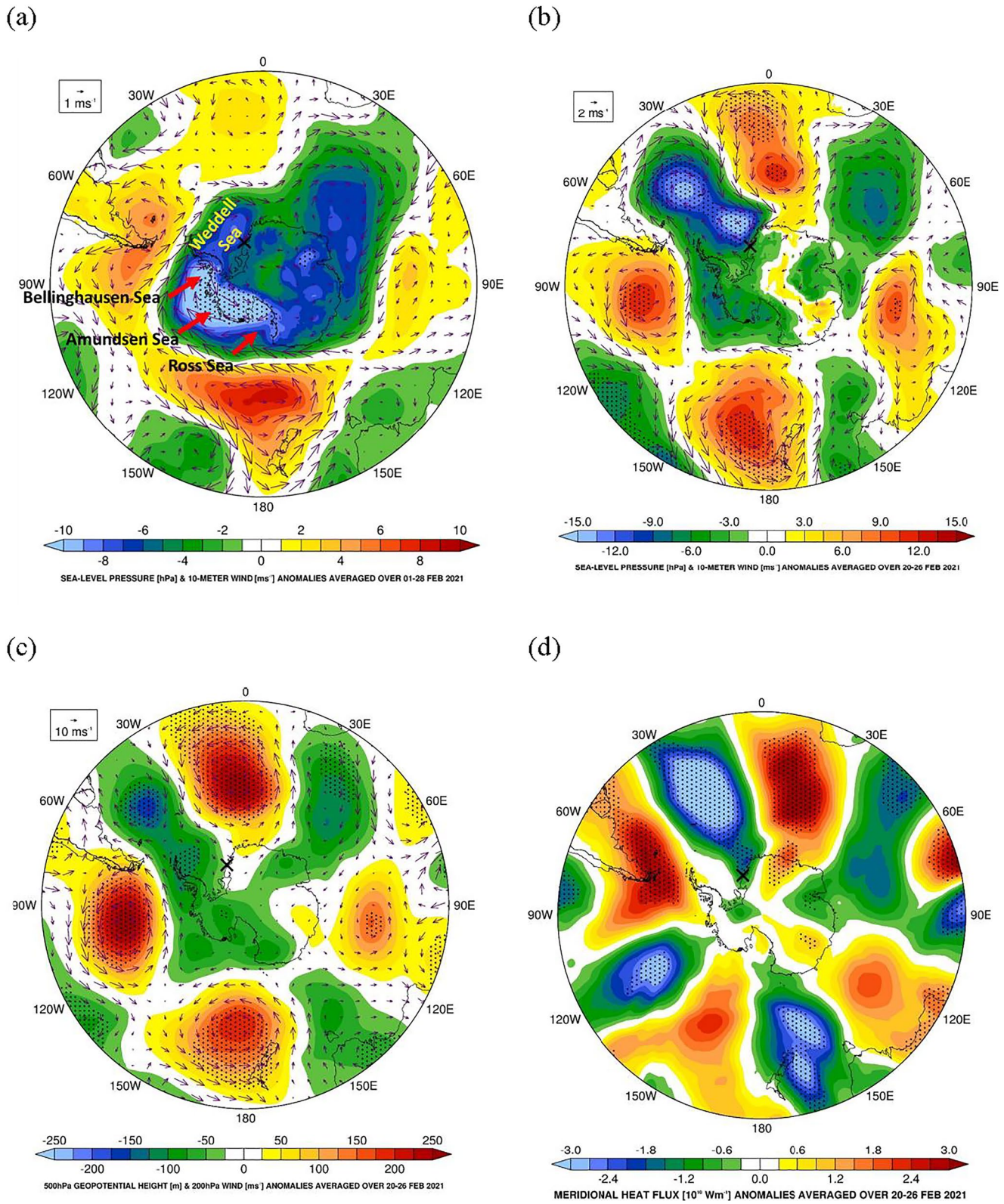

Figure 2.

anomalous low pressure generally develops over the Bellinghausen/Amundsen Sea during La Niña events in response to a wave train from lower latitudes which is triggered by changes in tropical SSTs and hence convection. The associated circulation favors warm and moist air advection from lower latitudes (and consequently reduced sea-ice concentration) in the Bellinghausen/Weddell Seas, and the opposite in the Ross/Amundsen Seas. The contrasting circulation between the Bellinghausen/Weddell Seas and the Ross/Amundsen Seas has been coined as the Antarctic Dipole (Yuan & Martinson, 2001). The ridge over and to the southeast of New Zealand, as well as the low pressure over the tropical Pacific, are also part of the atmospheric response to the La Niña (Kumar et al., 2010). A recent study by Goyal et al. (2021) further suggests that the zonal wavenumber three pattern, seen in Figure 2a, has a tropical origin and can impact the ice conditions around Antarctica (Maclennan & Lenaerts, 2021). Besides the La Niña, Figure 2a shows a poleward shift in the midlatitude storm track, as noted by the high pressure in the midlatitude and low pressure around Antarctica. This configuration corresponds to the positive phase of the Southern Annular Mode (SAM; Marshall, 2003), a mode of variability related to the strength and latitudinal position of the midlatitude westerly winds in the Southern Hemisphere. In fact, the SAM index for February 2021 was 2.19, which is more than 1 standard deviation above the 1979–2020 mean (0.04 ± 1.97). A combination of La Niña and a positive SAM has also been found to have promoted the September 1974 and 2017 polynya events in the Weddell Sea (Francis et al., 2020). It is important to note that this combination of ENSO and SAM phases is expected as La Niña events typically co-occur with positive SAM events (Fogt & Marshall, 2020).

A few days prior to the A-74 calving event (20–26 February 2021, Figure 2b), the La Niña signal noted above dominates the circulation (cf. Figure 2a), as evidenced by the anomalous low pressure over the Bellinghausen/Amundsen Seas, although there are some differences to the monthly mean anomaly (in particular in the South Atlantic sector): The low to the north of the BIS extends to 35°S just south of Uruguay, whereas in the monthly mean plot (Figure 2a) there is a ridge over the northern part of this region. The circulation associated with the sea-level pressure pattern (Figure 2b) draws in the moist and warm air from lower latitudes toward Antarctica, promoting intense cyclones and associated dynamical forcing (wind stress and turbulence) at the mouth of Antarctic ice shelves (Francis et al., 2020). This can be clearly seen in Figure 2d, which shows the meridional heat flux for the same period (negative values indicate southward/poleward transport of heat), with the anomalies being negative around the target region at 1 standard deviation below the mean.

It is interesting to note that the pressure anomalies in the South Atlantic in Figure 2b resemble those discussed in Rodrigues et al. (2015) in response to a central Pacific La Niña event, where the colder than average SST anomalies are restricted to the central equatorial Pacific (Ashok & Yamagata, 2009). The authors found that the tropical Pacific to South Atlantic teleconnection via a wave train that extends across South America is absent in ENSO events, which is the case for the 2020/2021 La Niña (Yu et al., 2022).

Figure 3 shows the outgoing longwave radiation (OLR; a proxy for convection in the tropics), the 200 hPa stream function anomalies and the 200 hPa *W* vectors (Takaya & Nakamura, 2001) averaged over 19–22 and 23–26 February. The tropical-extratropical interaction is more pronounced in the Northern Hemisphere due to the strong and equatorward-displaced subtropical jet (Sardeshmukh & Hoskins, 1988). However, in the Southern Hemisphere its impact can also be clearly seen, in particular over the central and eastern Pacific, where cross-hemispheric wave activity is present in line with theoretical arguments (Li et al., 2015). During the period 19–26 February, zonal wave propagation via troughs and ridges within the strong zonal wavenumber 3 pattern, dominates over poleward propagation of waves from the tropics. It is interesting to note that the zonal wavenumber 3 pattern and the high-amplitude storm track may have caused the convective burst to the northeast of New Zealand (180°–150°W, 5°–30°S), given by the negative OLR anomalies in Figures 3a and 3c which are indication of colder cloud tops and hence deep convection. During this period, there was a cyclone to the north of New Zealand (Figures 3b and 3d) which likely pushed a cold front into the tropics and triggered a band of convection, in a region where extratropical wave activity is known to modulate tropical convection (Matthews, 2012). It does appear that the convection in this region and the cyclone over the Weddell Sea occur from the same large-scale zonal wavenumber 3 (Figure 3d) and positive SAM pattern which were both favored by the ongoing La Niña. In the next section, the impact of local weather conditions just prior and during the time of calving are discussed.

Figure 2. (a) Sea-level pressure (shading; hPa) and 10-m horizontal wind (vectors; m s^{-1}) anomalies, with respect to the daily 1979–2020 climatology, averaged over 01–28 February 2021. The stipple denoted regions for which the sea-level pressure anomalies are more than 1 standard deviation away from the mean. (b) is as (a) but with the fields averaged over 20–26 February. (c) 500 hPa geopotential height (shading; m) and 200 hPa horizontal wind (vectors; m s^{-1}) anomalies and (d) meridional heat flux (10^{10} W m^{-1}; positive values indicate a flux from south to north) anomalies averaged over 20–26 February 2021. The cross in all panels indicates the approximate location of the Brunt Ice Shelf (BIS), while the Weddell, Ross, Amundsen, and Bellinghausen Seas are labeled in panel (a).

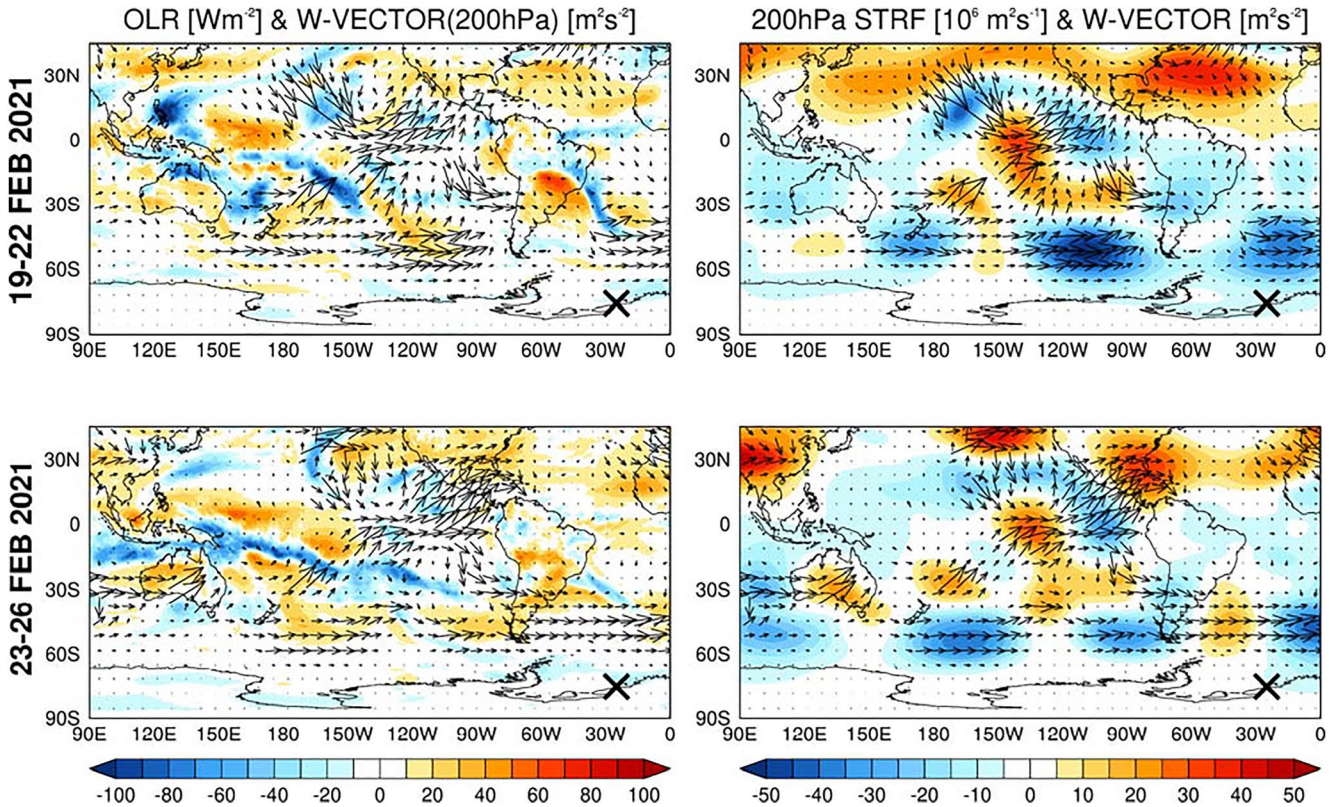

Figure 3. (a) Outgoing longwave radiation (shading; W m^{-2}) and 200 hPa *W* vectors (arrows; m^2 s^{-2}) averaged over 19–22 February 2021. (b) is as (a) but with the shading giving the 200 hPa stream function anomalies (106 m^2 s^{-1}) with respect to the 1979–2020 ERA-5 climatology. (c) and (d) are as (a) and (b) but with the fields averaged over 23–26 February 2021. The cross in all panels indicates the approximate location of the Brunt Ice Shelf (BIS).

4. Atmospheric Extremes at the BIS

The meteorological conditions around the BIS 1 week prior to the calving of the A-74 iceberg (i.e., on 20 February 2021) were characterized by a strong low-pressure system, stationed just to the northwest of the BIS paired with an intense atmospheric river (AR; an elongated band of clouds and high water-vapor content) to the northeast of the cyclone center (Figure 4a). Heavy snowfall fell over the BIS on 20–23 February with total hourly accumulation snowfall at 12 UTC of each day exceeding 0.5 mm water equivalent (mm we, Figure 5). As the 2-m temperature was around −5°C, the snowfall over BIS was most probably warm which could have destabilized the ice shelf further. However, an analysis of the mechanical influence of the snow accumulation on the ice shelf is beyond the scope of this study and worth to be investigated in future work.

Strong easterly winds (in excess of 20 m s^{-1}) over the BIS front resulting from the cyclone were fueled by the warm air brought by the AR. These surface winds were up to 3 standard deviations above the climatological mean and in the top 10% of the climatological range (Figure 4b). These extreme wind conditions may have led to high waves into the BIS front. When averaged over the BIS and the region around it, the wind speed on 20 February was in the top 1% of the range of values in the austral summer seasons of 1979–2020, with the speeds in excess of 20 m s^{-1} from 20 to 22 February being in top 5%, highlighting the extreme nature of the cyclone (Figure 6).

On 23 February, the deep cyclone moved eastwards and intensified, passing just to the north of the BIS (Figure 4c) with a minimum sea-level pressure of about 952 hPa. The meridional component of the wind around the ice shelf was offshore, and in particular on 24 February, had a magnitude that was in the top 5% of the climatological summertime values (Figure 6). These persistent strong southeasterly winds can create oceanward sea-surface slopes which were found to trigger calving events at other Antarctic ice shelves (i.e., the calving of the Amery Ice Shelf in 2019, Francis et al., 2021). The intense cyclone seen on 20 February (Figure 4b) persisted in the BIS region for 4 days. It started to weaken on 25 February as it propagated eastwards and gradually weakened and dissipated on 26 February (Figure 4d).

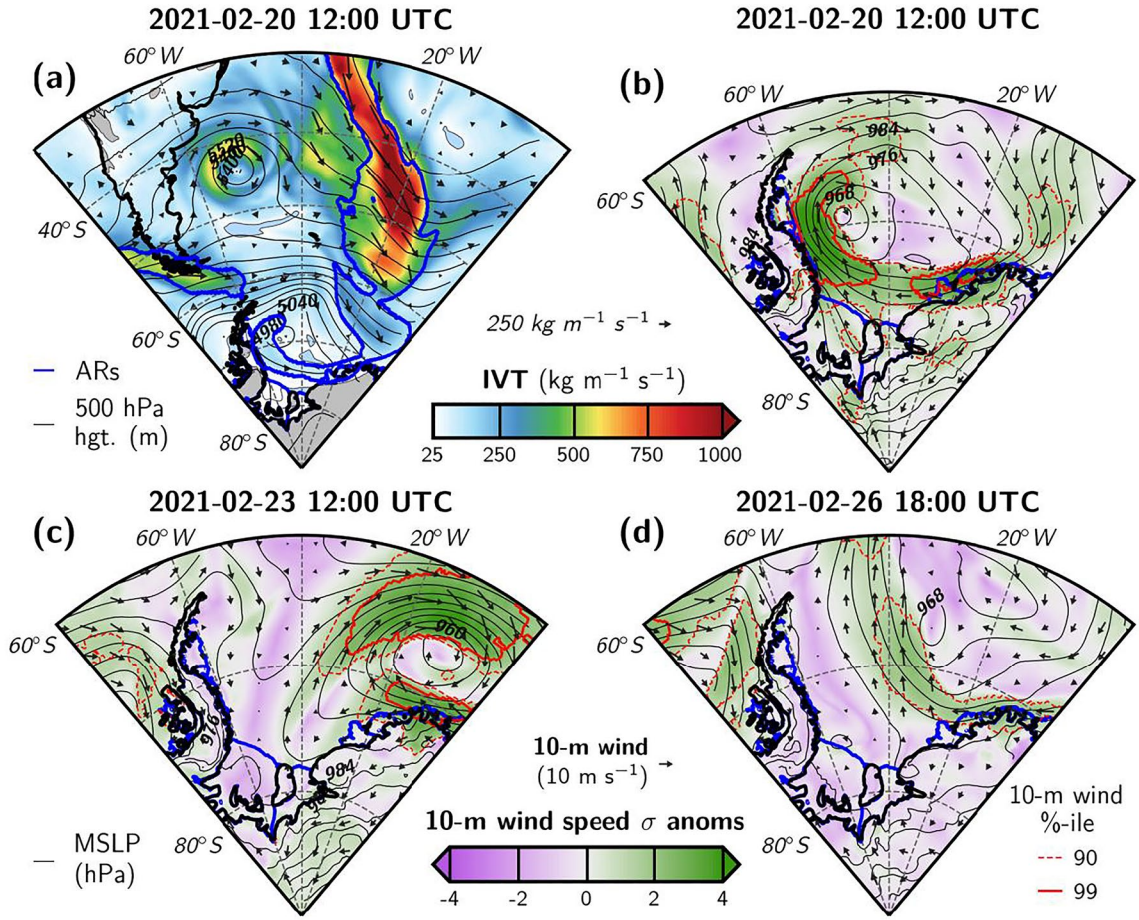

Figure 4. (a) Integrated Vapor Transport (IVT; arrows; kg m^{-1} s^{-1}), with the shading giving the magnitude, and 500 hPa geopotential height contours (solid lines, labeled every 60 m). The thick blue line identifies the atmospheric rivers (ARs) following Francis et al. (2020). (b–d) 10-m horizontal wind vectors (arrows; m s^{-1}), standardized wind speed anomalies (shading), and sea-level pressure (solid lines, labeled every 4 hPa). The dashed and solid red lines give the 90% and 99% percentile of the wind speed distribution, respectively. The solid blue line denotes the outlines of ice shelves, including the Brunt Ice Shelf (BIS). The fields are shown on (a) and (b) 20 February 2021 at 12 UTC, (c) 23 February 2021 at 00 UTC, and (d) 26 February 2021 at 18 UTC.

In situ observations at the Halley station located just to the southwest of the calving region provided insight on the local atmospheric conditions during the month of February 2021 (Figures 7a and 7b). The AR was associated with poleward advection of warm maritime air masses, consistent with the integrated water vapor (IWV) values of 6–7 kg m^{-2} (Figure 7c) and the air temperatures of −5°C around the calving location (Figure 7a). As seen in the time series plot (Figure 7b), the wind speed reached 15 m s^{-1} close to the calving region, with the easterly flow bringing in warmer and more moist lower-latitude air to the ice shelf: e.g., from 20 to 21 February, the air temperature increased by roughly 10°C and the IWV by 3 kg m^{-2}. Even more extreme weather conditions were observed from 12 to 16 February, in association with another deep cyclone that passed north of the BIS (Figure 7a). The warmer, moister, and cloudier environment led to an increase in the surface net radiation flux (R_{net}) to >+150 W m^{-2}, with the surface total energy flux (F_{net}) being positive during daytime and peaking at roughly +100 W m^{-2} on 21 February. While temperatures and moisture recorded at Halley station and over the BIS were relatively high, surface air temperatures did not exceed the surface melt threshold of −2°C (Nicholas et al., 2017) and therefore surface melt likely did not play a dominant role. However, surface melt may have occurred in some areas of the ice shelf given the favorable atmospheric conditions. In such case, rapid refreeze of any surface melt would have been possible and could have promoted hydrofracturing prior to the calving (e.g., Scambos et al., 2009). The peak values of R_{net} and F_{net} are similar to those reported by Francis et al. (2020) for the intense ARs that led to the melting of sea-ice and the opening of polynyas in the Weddell Sea in November 1973 and September 2017. As noted by Francis et al. (2021), extreme atmospheric conditions in polar regions can weaken an ice shelf due to the widening of existing fractures through wind-induced waves and swells.

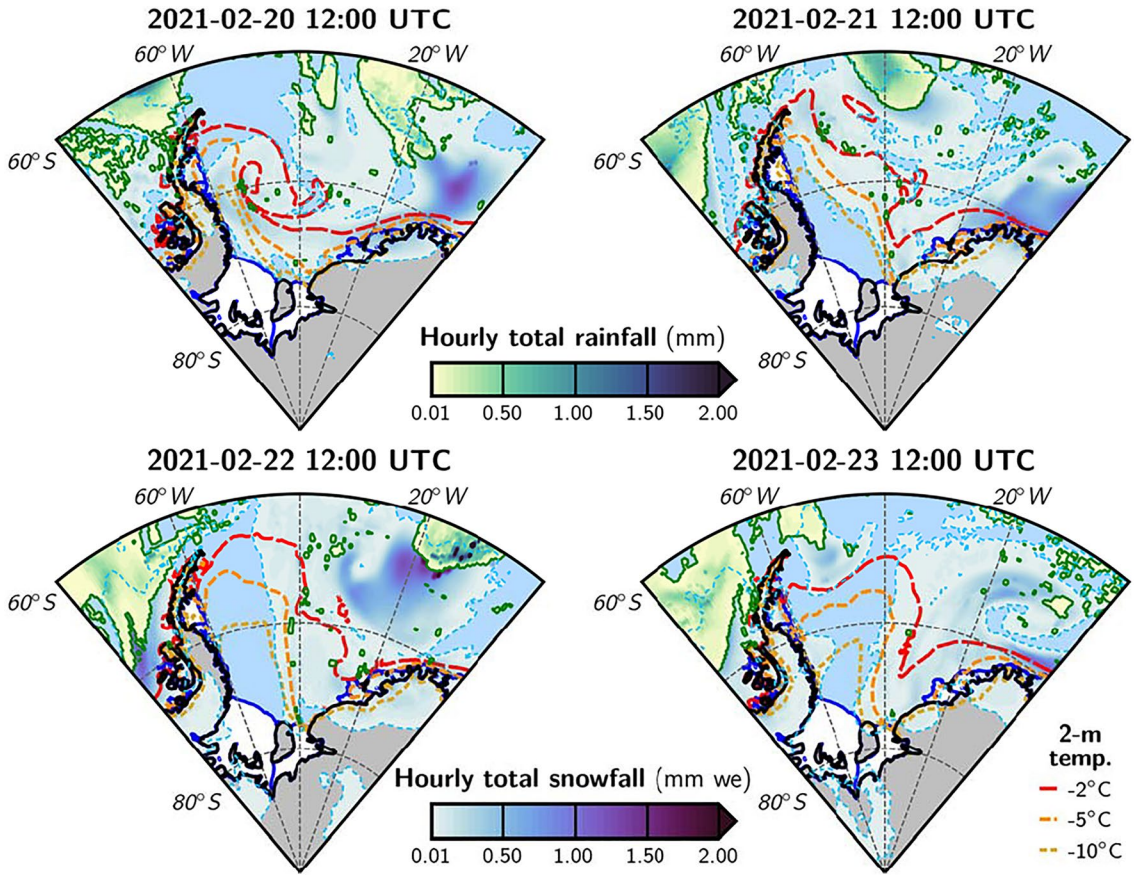

Figure 5. Hourly accumulated rainfall and snowfall from ERA5 at 12:00 UTC of each day from 20 February 2021 to 23 February 2021. Values are the total accumulated amount for the hour ending at 12:00 UTC, with accumulated snowfall in mm of water equivalent (mm we) for direct comparison with accumulated rainfall in mm. Also plotted are the −2, −5, and −10°C 2-m isotherms. The solid blue line highlights the outlines of ice shelves, including the Brunt Ice Shelf (BIS).

After the cyclone had moved to the east of the BIS, the clockwise circulation around its center generated extreme east-southeasterly (offshore) winds over the BIS front (Figure 6) which advected colder and drier air to the site: the air temperature and the IWV decreased to about −20°C and 3.5 kg m^{-2} on 26 February (Figures 7a and 7b), respectively. The sky was clearer as evidenced by the decrease in the surface downward longwave radiation flux by about 100 W m^{-2} with respect to 21–24 February (Figure 7c). These offshore winds, with speeds of around 14 m s^{-1} (Figure 7a), likely amplified existing fractures in the ice shelf via the increase in oceanward sea-surface slope (e.g., Francis et al., 2021), which contributed to the calving and then promoted the drift of the iceberg away from the ice shelf in early March 2021 (Figures 1c and 1d). This will be demonstrated in the next section, where the effects of the atmospheric conditions on the ocean slope and ice conditions will be investigated.

5. Effect of Atmospheric Forcing on Ocean Slope and Ice Conditions

The extreme atmospheric conditions discussed earlier resulted in high ocean slopes as shown in the time series of the maximum ocean slope around the BIS in the buildup to the calving event (Figure 8a). The ocean slope here refers to the horizontal gradient of the height of the water column, with larger values indicating higher water levels away from the ice shelf. The ocean slope is an important factor regulating the stability of the fronts of ice shelves as it modulates the stress endured by the front across the ocean-ice shelf boundary (Heywood et al., 2014).

While the slope was not particularly high on the day of the calving (0.03° on 26 February), the month of February 2021 was characterized by exceptionally high slopes, peaking at 0.068° on 24 February, the second consecutive day of strong southeasterly winds at the site (Figures 4 and 6). The map of maximum ocean slope anomaly in the second half of February 2021 with respect to the period April 2020 to March 2021 is shown in Figure 8a bottom panel. The values around the BIS just before and around the calving day were highly anomalous. The slopes

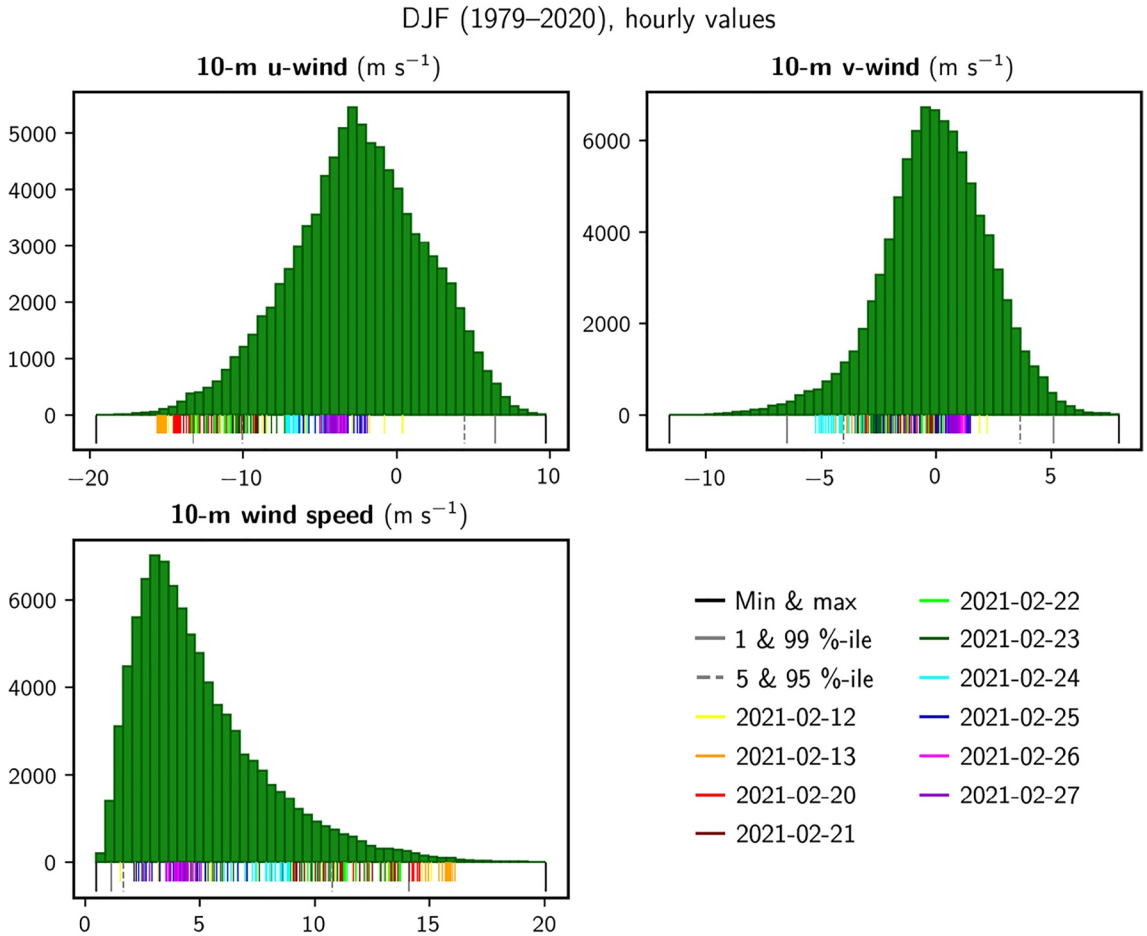

Figure 6. Histogram showing the distribution of hourly 10-m zonal, meridional and full horizontal wind speed (m s^{-1}) for the austral summer season (December to February, DJF) during 1979–2019, spatially averaged over the domain 24°–28°W and 74.8°–75.8°S. The colored vertical lines correspond to hourly values for selected days in the period 12–27 February 2021, labeled following the format *yyyy-mm-dd* where *yyyy* is the year, *mm* is the month, and *dd* is the day. The markers of same color on the *x*-axis show the hourly values on each day (24 markers per day). The dashed gray lines give the 5th and 95th percentiles, the solid gray lines give the 1st and 99th percentiles, while the solid black lines give the minimum and the maximum of the wind speed distribution.

calculated during the calving of the BIS in February 2021 are up to a factor of 2 higher than those estimated during the September 2019 break-up of iceberg D28 from the Amery Ice Shelf (Francis et al., 2021). These steep slopes added extra stress to the pre-existing rift in the ice shelf (Figures 1a and 1b) resulting in rift growth and leading to the calving.

The steep slopes not only promoted the calving, but also aided in the drifting of the iceberg A-74. The movement of ice can be visualized in Figure 8b, where the arrows give the direction of the displacement of the ice on 17 March 2021 with respect to that on 15 October 2020 as estimated from Landsat 8 satellite data (Fahnestock et al., 2016). The seaward displacement of the iceberg is clearly evident. Similarly, the behavior of the ice during the calving event can be seen in Figure 8c based on GPS measurements, labeled as HH00 in the map. The ice was moving at a rate of about 6 m day^{-1} before the calving, and immediately accelerated after the event. As a consequence of this acceleration its velocity was 2 orders of magnitude larger than before the calving; up to 700 m day^{-1}. The calving took place at 8 a.m. local time on 26 February 2021 and immediately afterward there was rotation in a clockwise direction. The final break happened at the eastern end of the rift (e.g., Libert et al., 2021). The clockwise rotation of the ice throughout the event is clearly seen in the MODIS images (Figure 1) and is consistent with a clockwise shift in the wind direction at Halley station (Figure 7b). While the winds at Halley were not particularly strong on 25–26 February not exceeding 5 m s^{-1} (Figure 7b), they were in the previous days with speeds of up to 15 m s^{-1} which indicates a latency of a few days between the strong winds and the ocean/ice response.

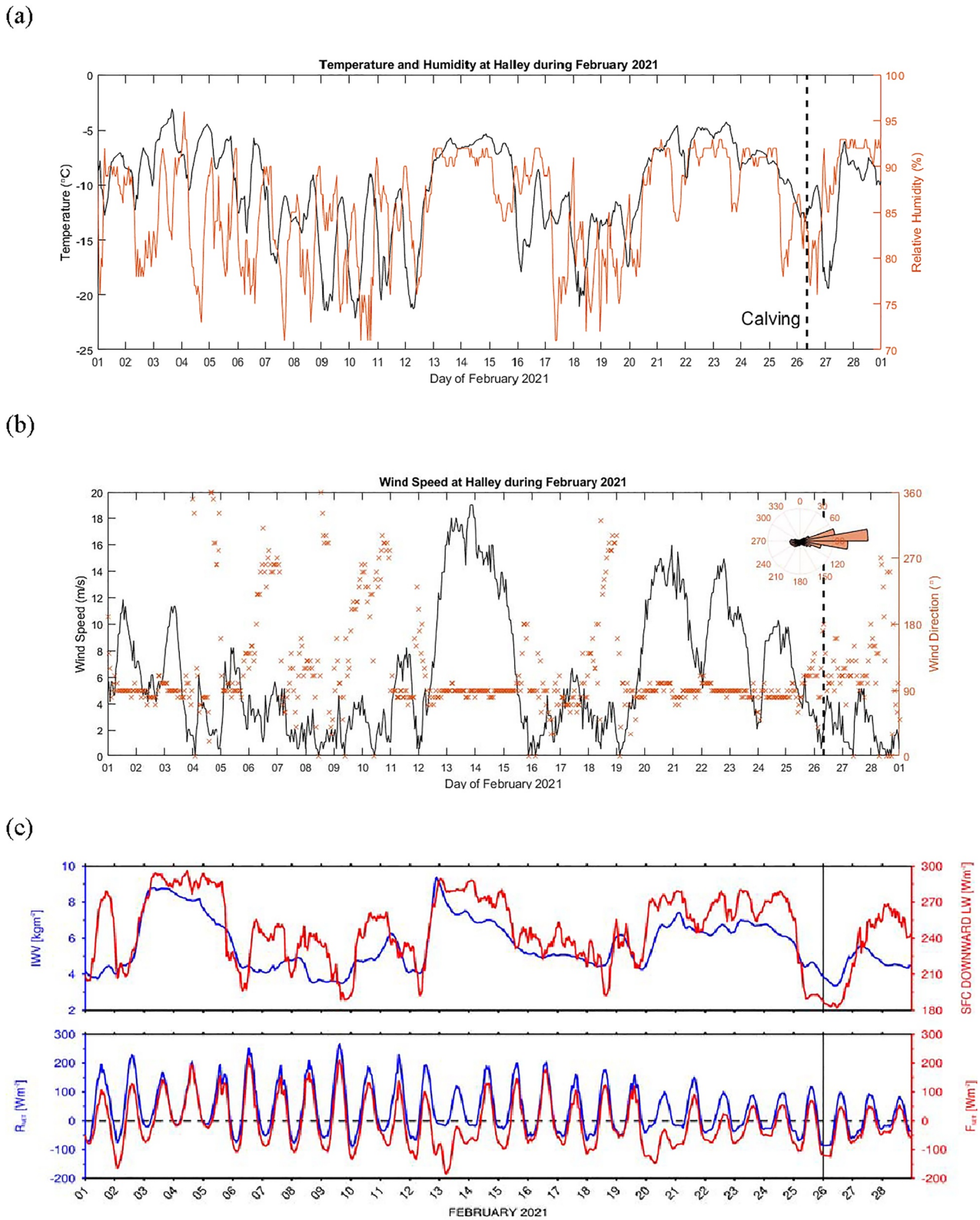

Figure 7. (a) Hourly 2-m temperature (°C) and relative humidity (%) and (b) 10-m wind speed (m s^{-1}), direction (°) and wind rose for February 2021 at the Halley Research Station (75.5681°S; 25.5083°W, Halley VIa in Figure 8c) on the Brunt Ice Shelf. (c) Integrated water vapor (kg m^{-2}) and surface downward longwave radiation flux (W m^{-2}), surface net radiation flux (R_{net}; W m^{-2}) and total energy flux (F_{net}; W m^{-2}) from ERA-5 averaged over 74.7°–75.7°S and 26.2°–25.2°W, a domain which comprises the location of the iceberg A-74 postcalving (75.217°S; 25.683°W) and the Halley station, for February 2021.

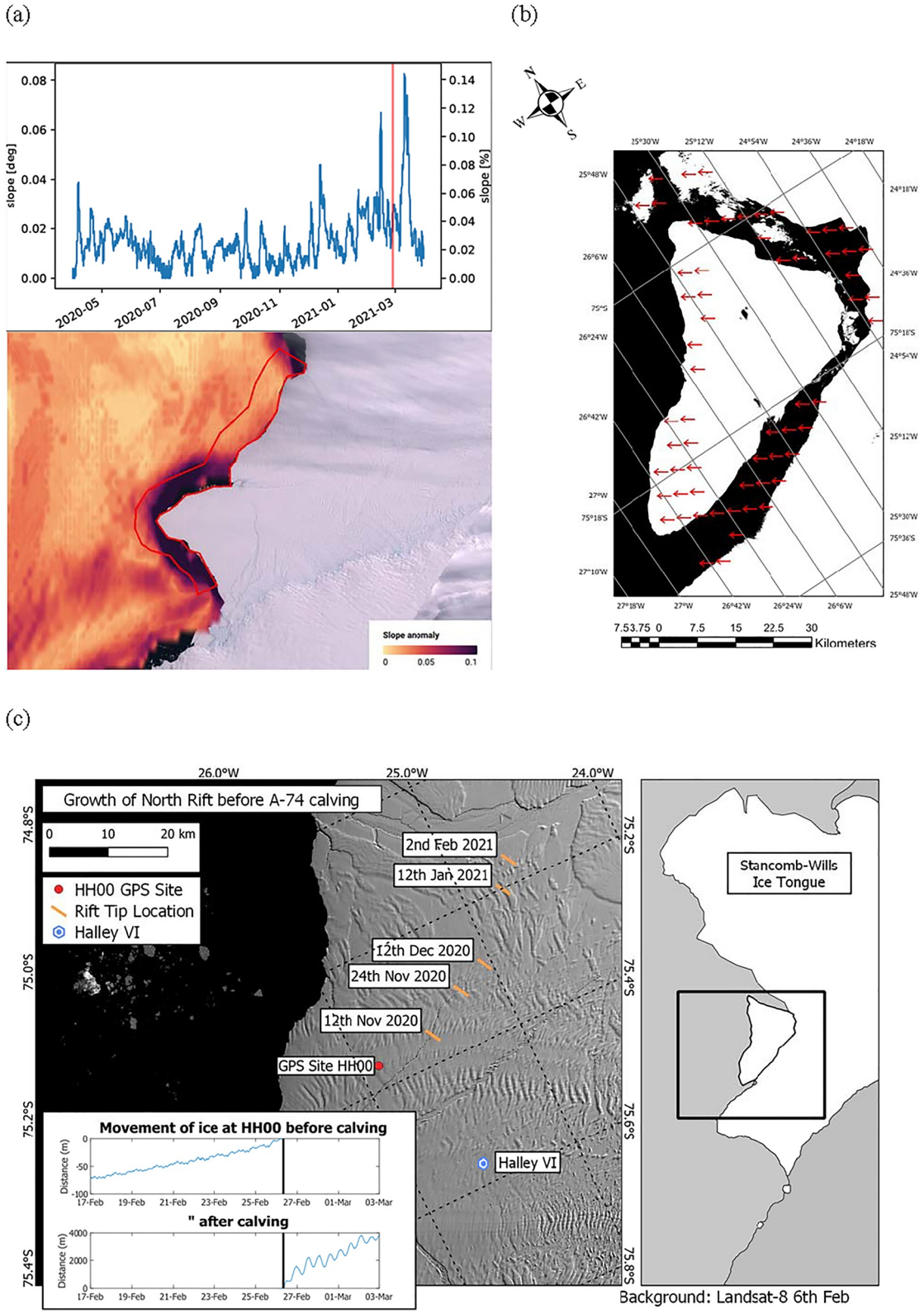

Figure 8.

In summary, the deep and persistent cyclone observed prior to the calving at the front of the BIS and which was associated with a strong ZW3 and positive SAM pattern, has provided the ideal conditions for the calving event through a two-phase process. During the first phase, the ice shelf was influenced by warm and moist air combined with high ocean waves and swells into the ice shelf which may have helped to fragilize the ice structure. During the second phase, strong offshore winds create high sea-surface slope toward the ocean forcing dynamically the ice shelf front to calve along the pre-existing rift after being weakened during the first phase. The switching from phase one (northeasterlies) to phase two (southeasterlies) occurs in a relatively short-time period (3 days), following the cyclone's position and trajectory.

6. Conclusions

In this study, the role of atmospheric forcing that triggered the calving of A-74 from the BIS in February 2021, and the subsequent drift of the 1,270 km^2 iceberg into the Southern Ocean, is investigated using a combination of observational and reanalysis products.

In the days preceding the calving, the region around the BIS experienced a pronounced advection of warmer and more moist lower-latitude air, with the meridional heat flux being more than 1 standard deviation above the mean. This poleward flux of heat was associated with a steep pressure gradient between a deep low located to the north and west of the ice shelf and a ridge to its east. This pressure dipole was likely a result of the atmospheric responses to the ongoing La Niña and positive SAM phase, which resulted in a strong zonal wavenumber 3 in the Southern Hemisphere midlatitudes.

At a regional scale, two periods of interest were identified: (a) 20–21 February, characterized by a strong easterly wind and (b) 23–24 February, when a deep low was situated to the northwest of the ice shelf generating strong offshore winds and leading to the calving. During the 20–21 February, as the low pressure sat to the northwest of the area, the associated easterly winds, up to 3 standard deviations above the mean, brought warmer (the air temperature increased by ∼10°C) and more moist (the IWV rose by ∼3 kg m^{-2}) air into the region through an AR. Wet snow also fell around the BIS, which may have further weakened the ice shelf. The poleward advection of low-latitude air continued and resulted in an increase in the surface total energy flux peaking at +100 W m^{-2}. As the cyclone shifted eastwards and sat to the north of the BIS front during 23–24 February, the wind turned southeasterly. This caused high sea-surface slope toward the open ocean which promoted the calving event, and the drift of the newly formed iceberg northwards.

In fact, as a result of the strong winds in the days prior to the calving, oceanward sea-surface slopes as high as 0.08° were seen in reanalysis data. Such values indicate a steep horizontal gradient in the height of the water column away from the shelf which dragged the ice shelf front away from the parent ice shelf along a pre-existing rift, stretching existing fractures and ultimately promoting its calving. Data from a GPS station located on the ice shelf revealed a 2 orders of magnitude increase in its velocity after the calving, with the iceberg moving away from the ice shelf at a speed of around 700 m day^{-1}. The clockwise rotation of the iceberg during the event is consistent with that of the wind direction at the Halley station located on the ice shelf.

In summary, the persistently strong cyclone observed prior to the calving event has provided the ideal conditions to trigger the calving event through a two-phase process. During the first phase, the ice shelf was influenced by warm and moist air and wet snow which resulted in an increase in the surface total energy flux. Combined with high ocean waves and swells, it may have helped to weaken the structure of the ice shelf front. During the second phase, strong offshore winds created high sea-surface slope toward the ocean forcing dynamically the ice shelf front to calve along the pre-existing rift after being weakened during the first phase. The switch from phase one (northeasterlies) to phase two (southeasterlies) occurs in a relatively short-time period (3 days) following the cyclone position and trajectory.

Figure 8. (a) Upper panel: Ocean slope in degrees (°) and slope ratio (%) both derived from the HYCOM; reanalysis data set during the period April 2020 to March 2021 over the domain highlighted with a red contour in the bottom panel. The red vertical line indicates the calving day (26 February 2021). Bottom panel: The ocean slope anomaly (°) for the period 15–28 February 2021 relative to April 2020 to March 2021. (b) Ice-displacement vectors (red arrows; only direction is given) for the area around the Brunt Ice Shelf (BIS) on 17 March 2021 relative to 15 October 2020 from the Landsat 8 satellite. The black shading indicates water while ice is shaded in white. (c) The movement of the ice immediately preceding and following the calving from the Global Positioning System (GPS) at site HH00. The "0" on the *y* axis of the inset in panel (c) is the position of GPS HH00 station at the time of calving. The orange markers represent the position of the tip of the rift on the dates indicated. The location of the Stancombe-Wills Ice Tongue is labeled so as to more easily identify the BIS in the satellite images.

Recent studies have found a poleward shift and strengthening of the Southern Hemisphere's eddy-driven jet in the last few decades in particular during the austral summer (e.g., Fogt & Marshall, 2020), which was mainly attributed to the ozone depletion. Despite ozone recovery in recent years and the expected reduction in these trends, global warming may cause a continued poleward shift/intensification of the storm track and hence more frequent stormy periods around Antarctica in the warmer months. Therefore, calving events, such as the one discussed in this paper, may occur more often in a warming world, with atmospheric forcing playing an increasingly important role in calving events of marine-terminating ice shelves, preconditioned by long-term glaciological and oceanic forcings. These results highlight the need for models and data sets used to assess and project Antarctic and Greenland ice-shelf dynamics and sea-level rise to account for both local and regional atmospheric conditions in order to better predict their evolution and dynamics.

Conflict of Interest

The authors declare no conflicts of interest relevant to this study.

Data Availability Statement

All the data used to generate the figures in this study has been uploaded to Francis et al. (2022; https://zenodo.org/record/6392413#.YkKc-yhBw2w). All data sources used are freely available from the following websites: (a) ERA-5 reanalysis data can be downloaded from the Copernicus' Climate Change Service website (Hersbach et al., 2018; https://climate.copernicus.eu/index.php/climate-reanalysis); (b) the Hybrid Coordinate Ocean Model (HYCOM; Chassignet, 2022) output is extracted from https://www.hycom.org/; (c) the Landsat data are obtained from the United States Geological Survey's website (Applegate, 2022; https://earthexplorer.usgs.gov/); (d) the Moderate Resolution Imaging Spectroradiometer (MODIS) images were downloaded from the National Aeronautic and Space Administration's Worldview application (Boller, 2022; https://worldview.earthdata.nasa.gov); (e) the ground-based meteorological data at the Brunt Ice Shelf were acquired by the British Antarctic Survey and are available at http://basmet.nerc-bas.ac.uk/sos/ (Colwell, 2022). All figures were generated using the Interactive Data Language (IDL; Bowman, 2005; https://www.l3harrisgeospatial.com/Software-Technology/IDL) software version 8.8.1, and the Matplotlib (Hunter, 2007) version 3.5.1 available at https://matplotlib.org/.

Acknowledgments
The authors would like to acknowledge the contribution of Khalifa University's high-performance computing and research computing facilities to the results of this research. We would also like to thank two anonymous reviewers for their several insightful comments and suggestions which helped to significantly improve the manuscript. This work was funded by Masdar Abu Dhabi Future Energy Company.

References

Alley, R. B., Horgan, H. J., Joughin, I., Cuffey, K. M., Dupont, T. K., Parizek, B. R., et al. (2008). A simple law for ice-shelf calving. *Science*, *322*(5906), 1344. https://doi.org/10.1126/science.1162543

Applegate, D. (2022). United States Geological Survey (USGS) Earth Explorer. [Data Set]. USGS. Retrieved from https://earthexplorer.usgs.gov/

Ashok, K., & Yamagata, T. (2009). The El Nino with a difference. *Nature*, *461*, 481–484. https://doi.org/10.1038/461481a

Benn, D. I., Warren, C. R., & Mottram, R. H. (2007). Calving processes and the dynamics of calving glaciers. *Earth-Science Reviews*, *82*(3–4), 143–179. https://doi.org/10.1016/j.earscirev.2007.02.002

Boller, R. (2022). National Aeronautics and Space Administration (NASA) Worldview. [Data Set]. NASA. Retrieved from https://worldview.earthdata.nasa.gov/

Bowman, K. P. (2005). An introduction to programming with IDL: Interactive Data Language. [Software]. Academic *Pre*ss, 304. ISBN -10: 012088559X, ISBN-13: 978-0120885596 https://www.l3harrisgeospatial.com/Software-Technology/IDL

CChassignet, E. (2022). Hybrid Coordinate Ocean Model (HYCOM). Consortium for data assimilative modeling. Retrieved from https://www.hycom.org/

Colwell, S. (2022). British Antarctic Survey Sensor Observation Service—Meteorological data. [Data Set]. British Antarctic Survey. Retrieved from http://basmet.nerc-bas.ac.uk/sos/

Cook, A. J., Holland, P. R., Meredith, M. P., Murray, T., Luckman, A., & Vaughan, D. G. (2016). Ocean forcing of glacier retreat in the Western Antarctic Peninsula. *Science*, *353*(6296), 283–286. https://doi.org/10.1126/science.aae0017

Cook, A. J., & Vaughan, D. G. (2010). Overview of areal changes of the ice shelves on the Antarctic Peninsula over the past 50 years. *The Cryosphere*, *4*, 77–98. https://doi.org/10.5194/tc-4-77-2010

Cummings, J. A., & Smedstad, O. M. (2013). Variational data analysis for the global ocean. In S. Park, & L. Xu (Eds.), *Data assimilation for atmospheric, oceanic and hydrological applications* (Vol. III, pp. 303–343). Berlin Heidelberg: Springer-Verlag. https://doi.org/10.1007/978-3-642-35088-7_13

De Rydt, J., Gudmundsson, G. H., Nagler, T., & Wuite, J. (2019). Calving cycle of the brunt ice shelf, Antarctica, driven by changes in ice shelf geometry. *The Cryosphere*, *13*, 2771–2787. https://doi.org/10.5194/tc-13-2771-2019

Dong, X., Wang, Y., Hou, S., Ding, M., Yin, B., & Zhang, Y. (2020). Robustness of the recent global atmospheric reanalyses for Antarctic near-surface wind speed climatology. *Journal of Climate*, *33*(10), 4027–4043. https://doi.org/10.1175/jcli-d-19-0648.1

Fahnestock, M., Scambos, T., Moon, T., Gardner, A., Haran, T., & Klinger, M. (2016). Rapid large-area mapping of ice flow using Landsat 8. *Remote Sensing of the Environment*, *185*, 84–94. https://doi.org/10.1016/j.rse.2015.11.023

Fogt, R. K., & Marshall, G. J. (2020). The southern annular mode: Variability, trends, and climate impacts across the southern Hemisphere. *WIREs Climate Change*, *11*, e652. https://doi.org/10.1002/wcc.652

Francis, D., Eayrs, C., Cuesta, J., & Holland, D. (2019). Polar cyclones at the origin of the reoccurrence of the Maud Rise Polynya in austral winter 2017. *Journal of Geophysical Research: Atmospheres*, *124*, 5251–5267. https://doi.org/10.1029/2019JD030618

Francis, D., Fonseca, R., Mattingly, K. S., Marsh, O. J., Lhermitte, S., & Cherif, C. (2022). Datasets for publication "Atmospheric triggers of the Brunt Ice Shelf calving in February 2021". [Data Set]. Zenodo. Retrieved from https://zenodo.org/record/6392413#.YkKc-yhBw2w

Francis, D., Mattingly, K., Temimi, M., Massom, R., & Heil, P. (2020). On the crucial role of atmospheric rivers in the two major Weddell Polynya events in 1973 and 2017 in Antarctica. *Science Advances*, *6*(46), eabc2695. https://doi.org/10.1126/sciadv.abc2695

Francis, D., Mattingly, K. S., Lhermitte, S., Temimi, M., & Heil, P. (2021). Atmospheric extremes triggered the biggest calving event in more than 50 years at the Amery Ice Shelf in September 2019. *The Cryosphere*, *15*, 2147–2165. https://doi.org/10.5194/tc-2020-219

Gilbert, E., & Kittel, C. (2021). Surface melt and runoff on Antarctic ice shelves at 1.5°C, 2°C, and 4°C of future warming. *Geophysical Research Letters*, *48*, e2020GL091733. https://doi.org/10.1029/2020GL091733

Goyal, R., Jucker, M., Gupta, A. S., Hendon, H. H., & England, M. H. (2021). Zonal wave 3 pattern in the Southern Hemisphere generated by tropical convection. *Nature Geosciences*, *14*, 732–738. https://doi.org/10.1038/s41561-021-00811-3

Gwyther, D. E., Kusahara, K., Asay-Davis, X. S., Dinniman, M. S., & Galton-Fenzi, B. K. (2020). Vertical processes and resolution impact ice shelf basal melting: A multi-model study. *Ocean Modelling*, *147*, 101569. https://doi.org/10.1016/j.ocemod.2020.101569

Hersbach, H., Bell, B., Berrisford, P., Biavati, G., Horanyi, A., Munoz Sabater, J., et al. (2018). ERA5 hourly data on pressure levels from 1979 to present. [Data Set]. Copernicus Climate Change Service (C3S) Climate Data Store (CDS). https://doi.org/10.24381/cds.bd0915c6

Hersbach, H., Bell, B., Berrisford, P., Dahlgren, P., Horanyi, A., Munoz-Sebater, J., et al. (2020). *The ERA5 global reanalysis: Achieving a detailed record of the climate and weather for the past 70 years*. Vienna, Austria: European Geophysical Union General Assembly 2020. https://doi.org/10.5194/egusphere-egu2020-10375

Heywood, K. J., Schmidtko, S., Heuzé, C., Kaiser, J., Jickells, T. D., Queste, B. Y., et al. (2014). Ocean processes at the Antarctic continental slope. *Philosophical Transactions of the Royal Society A*, *372*, 20130047. https://doi.org/10.1098/rsta.2013.0047

Hogg, A., & Gudmudsson, G. H. (2017). Impacts of the Larsen-C ice shelf calving event. *Nature Climate Change*, *7*, 540–542. https://doi.org/10.1038/nclimate3359

Hunter, J. (2007). Matplotlib: A 2D graphics environment. [Software]. Computing in Science and Engineering, *9*, 90–95. https://doi.org/10.1109/MCSE.2007.55

Kumar, A., Jha, B., & L'Heureux, M. (2010). Are tropical SST trends changing the global teleconnection during La Niña. *Geophysical Research Letters*, *37*, L12702. https://doi.org/10.1029/2010GL043394

Larter, R. D. (2022). Basal melting, roughness and structural integrity of ice shelves. *Geophysical Research Letters*, *49*, e2021GL097421. https://doi.org/10.1029/2021GL097421

Lhermitte, S., Sun, S., Shuman, C., Wouters, B., Pattyn, F., Wuite, J., et al. (2020). Damage accelerates ice shelf instability and mass loss in Amundsen Sea Embayment. *Proceedings of the National Academy of Sciences of the United States of America*, *117*, 24735–24741. https://doi.org/10.1073/pnas.1912890117

Li, Y., Li, J., Jin, F.-F., & Zhao, S. (2015). Interhemispheric propagation of stationary Rossby waves in a horizontally nonuniform background flow. *Journal of the Atmospheric Sciences*, *72*(8), 3233–3256. https://doi.org/10.1175/jas-d-14-0239.1

Libert, L., Wuite, J., & Nagler, T. (2021). Automatic delineation of cracks with sentinel-1 interferometry for monitoring ice shelf damages and calving. [Preprint]. The Cryosphere Discuss. https://doi.org/10.5194/tc-2021-296

Maclennan, M. L., & Lenaerts, J. T. M. (2021). Large-scale atmospheric drivers of snowfall over Thwaites Glacier, Antarctica. *Geophysical Research Letters*, *48*, e2021GL093644. https://doi.org/10.1029/2021GL093644

Marshall, G. J. (2003). Trends in the Southern Annular Mode from observations and reanalyses. *Journal of Climate*, *16*, 4134–4143. https://doi.org/10.1175/1520-0442(2003)016<4134:titsam>2.0.co;2

Massom, R. A., Scambos, T. A., Bennetts, L. G., Reid, P., Squire, V. A., & Stammerjohn, S. E. (2018). Antarctic ice shelf disintegration triggered by sea ice loss and ocean swell. *Nature*, *538*, 383–389. https://doi.org/10.1038/s41586-018-0212-1

Matthews, A. J. (2012). A multiscale framework for the origin and variability of the South Pacific Convergence Zone. *Quarterly Journal of the Royal Meteorological Society*, *138*, 1165–1178. https://doi.org/10.1002/qj.1870

Nicolas, J. P., Vogelmann, A. M., Scott, R. C., Wilson, A. B., Cadeddu, M. P., Bromwich, D. H., et al. (2017). January 2016 extensive summer melt in West Antarctica favoured by strong El Nino. *Nature Communications*, *8*, 15799. https://doi.org/10.1038/ncomms15799

Paolo, F. S., Fricker, H., & Padman, L. (2015). Volume loss from Antarctic ice shelves is accelerating. *Science*, *348*(6232), 327–331. https://doi.org/10.1126/science.aaa0940

Rasmusson, E., & Carpenter, T. (1982). Variation in tropical sea surface temperature and surface wind fields associated with the Southern Oscillation/El Niño. *Monthly Weather Review*, *110*, 354–384. https://doi.org/10.1175/1520-0493(1982)110<0354:vitsst>2.0.co;2

Rignot, E., Jacbos, S., Mouginot, J., & Scheuchl, B. (2013). Ice-shelf melting around Antarctica. *Science*, *341*(6143), 266–270. https://doi.org/10.1126/science.1235798

Rodrigues, R. R., Campos, E. J. D., & Haarsma, R. (2015). The impact of ENSO on the South Atlantic subtropical dipole model. *Journal of Climate*, *28*(7), 2691–2705.

Rott, H., Skvarca, P., & Nagler, T. (1996). Rapid collapse of northern Larsen ice shelf, Antarctica. *Science*, *271*(5250), 788–792. https://doi.org/10.1126/science.271.5250.788

Sardeshmukh, P. D., & Hoskins, B. J. (1988). The generation of global rotational flow by steady idealized tropical divergence. *Journal of Atmospheric Sciences*, *45*(7), 1228–1251. https://doi.org/10.1175/1520-0469(1988)045<1228:tgogrf>2.0.co;2

Scambos, T., Fricker, H. A., Liu, C.-C., Bohlander, J., Fastook, J., Sargent, A., et al. (2009). Ice shelf disintegration by plate bending and hydro-fracture: Satellite observations and model results of the 2008 Wilkins ice shelf break-ups. *Earth and Planetary Science Letters*, *280*(1–4), 51–60. https://doi.org/10.1016/j.epsl.2008.12.027

Scambos, T., Hulbe, C., & Fahnestock, M. (2003). Climate-induced ice shelf disintegration in the Antarctic Peninsula. In E. Domack, A. Levente, A. Burnet, R. Bindschadler, P. Convey, & M. Kirby (Eds.), *Antarctic Peninsula climate variability: Historical and paleoenvironmental perspectives*. https://doi.org/10.1029/AR079p0079

Scambos, T., Hulbe, C., Fahnestock, M., & Bohlander, J. (2000). The link between climate warming and break-up of ice shelves in the Antarctic Peninsula. *Journal of Glaciology*, *46*(154), 516–530. https://doi.org/10.3189/172756500781833043

Simpkins, G. R., Ciasto, L. M., Thompson, D. W. J., & England, M. H. (2012). Seasonal relationships between large-scale climate variability and Antarctic sea ice concentration. *Journal of Climate*, *25*(16), 5451–5469. https://doi.org/10.1175/jcli-d-11-00367.1

Stammerjohn, S., Scambos, T. A., Adusumilli, S., Barreira, S., Bernhard, G. H., Bozkurt, D., et al. (2021). Antarctica and the Southern Ocean. *Bulletin of the American Meteorological Society*, *102*(8), 317–356. https://doi.org/10.1175/bams-d-21-0081.1

Stewart, C. L., Christoffersen, P., Nicholls, K. W., Williams, M. J. M., & Dowdeswell, J. A. (2019). Basal melting of Ross Ice Shelf from solar heat absorption in ice-front polynya. *Nature Geosciences*, *12*, 435–440. https://doi.org/10.1038/s41561-019-0356-0

Takaya, K., & Nakamura, H. (2001). A formulation of a phase-independent wave-activity flux for stationary and migratory quasigeostrophic eddies on a zonally varying basic flow. *Journal of Atmospheric Sciences*, *58*, 608–627. https://doi.org/10.1175/1520-0469(2001)058<0608:afoapi>2.0.co;2

Tian, Y., Hao, M., & Zhang, H. (2020). Unsupervised change detection using spectrum-trend and shape similarity measure. *Remote Sensing*, *12*(21), 3606. https://doi.org/10.3390/rs12213606

Wadhams, P., & Munk, M. (2004). Ocean freshening, sea level rising, sea ice melting. *Geophysical Research Letters*, *31*, L11311. https://doi.org/10.1029/2004GL020039

Xiong, X., & Barnes, W. (2006). An overview of MODIS radiometric calibration and characterization. *Advances in Atmospheric Sciences*, *23*, 69–79. https://doi.org/10.1007/s00376-006-0008-3

Yu, Y., Li, Y., Ren, R., Cai, M., Guan, Z., & Huang, W. (2022). An isentropic mass circulation view on the extreme cold events in the 2020/21 winter. *Advances in Atmospheric Sciences*, *39*, 647–657. https://doi.org/10.1007/s00376-021-1289-2

Yuan, X. (2004). ENSO-related impacts on Antarctic Sea Ice: A synthesis of phenomenon and mechanisms. *Antarctic Science*, *16*(4), 415–425. https://doi.org/10.1017/S0954102004002238

Yuan, X., & Martinson, D. G. (2001). The Antarctic dipole and its predictability. *Geophysical Research Letters*, *28*, 3609–3612. https://doi.org/10.1029/2001GL012969